Journal of Alloys and Compounds 805 (2019) 180–188

Contents lists available at ScienceDirect

Journal of Alloys and Compounds

journal homepage: http://www.elsevier.com/locate/jalcom

High performance $In_2(MoO_4)_3$@In_2O_3 nanocomposites gas sensor with long-term stability

Feng-Hua Zhang [a, b, 1], Yu-Chong Wang [a, 1], Lei Wang [c], Jian Liu [d], Hong-Liang Ge [e], Bin Wang [a], Xin-Yu Huang [a], Xue-Dong Wang [f, **], Zong-Tao Chi [a, ***], Wan-Feng Xie [a, b, e, *]

[a] School of Electronics & Information Engineering, Qingdao University, Qingdao, 266071, China
[b] School of Physics, Shandong University, Jinan, 250100, China
[c] Key Laboratory of Engineering Earthquake, Shandong Earthquake Agency, Jinan, 250102, China
[d] State Key Laboratory of Solid Lubrication, Lanzhou Institute of Chemical Physics, Chinese Academy of Sciences, Lanzhou, 730000, China
[e] School of Chemistry and Chemical Engineering, Shandong University, Jinan, 250100, China
[f] Jiangsu Key Laboratory for Carbon-Based Functional Materials & Devices, Institute of Functional Nano & Soft Materials (FUNSOM), Soochow University, Suzhou, Jiangsu, 215123, China

ARTICLE INFO

Article history:
Received 4 April 2019
Received in revised form
21 June 2019
Accepted 28 June 2019
Available online 4 July 2019

Keywords:
Metal oxide semiconductor
$In_2(MoO_4)_3$
Sensing
Hydrothermal
Humidity

ABSTRACT

Metal oxide semiconductor (MOSC) sensors based on nanocrystalline MoO_3, In_2O_3, and their composites are considered to be very sensitive to detect low concentrations of ethanol, ozone, hydrogen, formaldehyde, and nitrogen dioxide. Here, we firstly introduced $In_2(MoO_4)_3$ phase, which has excellent negative thermal expansion and high electric conductivity properties, into $In_2(MoO_4)_3$@In_2O_3 crystalline nanocomposites. The gas-sensing performance of the $In_2(MoO_4)_3$@In_2O_3 nanocomposites was studied upon exposure to the ethanol gas with different concentration from 5 to 300 ppm at the optimum temperature (300 °C). What's more, the device possesses ultra-high response of 110 and selectivity to ethanol. Particularly, it can effectively work in high humidity (RH = 80%) with super long-term stability of as long as 90 days, compared with the pristine In_2O_3 sensor and previous reports. The presented novel $In_2(MoO_4)_3$@In_2O_3 sensor offers great opportunities for future ethanol detection under harsh conditions.

1. Introduction

Metal oxide semiconductor (MOSC) is a very important material, which extensively utilized in various fields such as gas sensors [1–4], field effect transistors (FETs) [5], solar cells [6], secondary batteries [7], dielectric metasurfaces [8], display [9], and in a number of other applications including superconductor [10]. In recent years, MOSC gas sensors, such as MoO_3, In_2O_3, TiO_2, SnO_2, WO_3, ZnO, α-Fe_2O_3, and their nanocomposites based have drawn numerous interests due to their domestic and industrial applications for detection of irritative gases, explosive gases, toxic gases, and volatile organic compounds (VOC) [11–14]. Depending on the current mechanism of gas sensor, the detected gas can induce a resistance increase of the device on *n*-type semiconductor oxides. The increased resistance can be attributed to surface processes, and explained in terms of capturing free electrons from the conduction band (E_c) of the semiconductor by adsorbed target gas [13,14]. Take reducing ethanol gas as an example, the absorbed ethanol molecule can break down into two CO_2, one H_2O and 6 electrons (6 e^{-1}) due to the lower bond energy of C–C in ethanol, and the 6 e^{-1} lead to an abrupt alteration of device's resistance [11,14–17].

In a wide variety of MOSC nanomaterials, MoO_3, In_2O_3 and their composites exhibit high sensitivity and short response time, according to the literature, and in these aspects much better than other sensing materials. In 2014, for example, the two-dimensional (2D) molybdenum oxide flakes were obtained by grinding-assisted liquid exfoliation method, and exhibits ultra-high H_2 gas sensing performance [18]. In 2015, Feng and his coworkers synthesized In_2O_3-WO_3 heterojunction nanofibers, which had good gas sensing properties [19]. Then, Ji and his co-workers obtained 2D MoO_3 nanosheets by grinding and sonication processes, the chemical sensor performance have significant enhancement such as

* Corresponding author. School of Electronics & Information Engineering, Qingdao University, Qingdao, 266071, China.
** Corresponding author.
*** Corresponding author.
E-mail addresses: wangxuedong@suda.edu.cn (X.-D. Wang), zoc545s@163.com (Z.-T. Chi), wfxie@qdu.edu.cn (W.-F. Xie).
[1] These two authors contribute equally.

https://doi.org/10.1016/j.jallcom.2019.06.369
0925-8388/

response is 33, the response time is 21 s, and the recovery time is 10 s [20]. In addition, Sabolsky et al. reported that the micro & nano particulate of $SrMoO_4$ exhibited excellent promise in sensitivity, stability and selectivity to SO_2 up to 1000 °C [21]. In 2017, Microfibers of $SrMoO_4$/MgO were synthesized via a two-step hydrothermal approach, and exhibited showed selective detection of hydrogen (H_2) up to 1000 °C with high sensor response and stability for the given concentrations [22]. Afterwards, Wang's group reported that the α-MoO_3/$Fe_2(MoO_4)_3$ nanocomposites exhibited enhanced sensing response and selectivity to toluene vapor compared to bare α-MoO_3 nanobelts at the optimal operating temperature of 250 °C [23]. In 2018, Fan's group reported that the In_2O_3 hollow microtubules were fabricated by using degreasing cotton as soft bio-templates, and the gas response of the In_2O_3 hollow microtubules sensor was 1051 to 10 ppm Cl_2 at 200 °C, which was 25 times higher than In_2O_3 particles [24]. Altogether, In_2O_3/MoO_3 nanocomposites attracted much scientific interests in various areas due to the high conductivity of In_2O_3 and low cost of MoO_3, in particularly, the MoO_3/In_2O_3 based gas sensors shows good gas sensing properties such as higher sensitivity, faster response/recovery times. Though good results have been achieved on MoO_3, In_2O_3 and their composites based sensors, to the best of our knowledge, the gas sensing properties of long term stability has been barely investigated, and especially it can run effectively in harsh conditions such as high humidity. Therefore, a superior gas sensor with long-term stability is highly desirable in practical applications.

Binary and ternary metal oxide systems have been subjects of intense interest as their characterization is essential for the design of new materials of different types, like semiconductors, magnetic and optical materials or construction materials of specific thermal, mechanical or chemical properties [23,25,26]. In accordance to the recent findings, $In_2(MoO_4)_3$, as an outstanding functional material, has been investigated and applied in many areas such as electrolyte in fuel cells, laser materials, and lithium storage due to negative thermal expansion and high electric conductivity [25–27]. Recently, $Fe_2(MoO_4)_3$ has been identified as a potential candidate for gas sensing [28,29]. However, to date, $In_2(MoO_4)_3$ and its composites toward to ethanol have been scarcely reported. Herein, we firstly design and combine $In_2(MoO_4)_3$ and In_2O_3 together to fabricate a promising material for improving the gas sensing performance towards ethanol. The obtained $In_2(MoO_4)_3$@In_2O_3 nanocomposites have peony-like nanostructure, and the $In_2(MoO_4)_3$@In_2O_3 sensor possesses ultrahigh response and selectivity to ethanol. Especially, the home-made devices can run effectively with long term stability under harsh conditions.

2. Experimental

2.1. Materials

Indium chloride, ammonium molybdate, thiourea, ammonium fluoride, citric acid, sodium hydroxide and absolute ethyl alcohol were purchased from Aladdin (Shanghai, China). All the reagents that we used were of analytical grade and utilized directly without further purification.

2.2. Preparation of $In_2(MoO_4)_3$@In_2O_3 nanocomposites

The $In_2(MoO_4)_3$@In_2O_3 nanocomposites was successfully synthesized by the following processes. Typically, 5 mmol ammonium molybdate, 30 mmol thiourea and 5 mmol ammonium fluoride were dissolved in 50 mL distilled water firstly, and followed vigorous stirring for 30 min. Subsequently, 2 mmol citric acid was added to the above solution, and then the obtained solution was transferred into a 60 mL Teflon-lined autoclave with the heating at 200 °C for 24 h. Afterwards, the obtained MoS_2 suspension was washed several times with absolute ethanol and deionized water to remove redundant ions, upon ultrasonicating for 10 min and centrifuging at 6900 rpm for 30 min, respectively. After dried at 80 °C for overnight in vacuum drying chamber, the black MoS_2 powder was obtained. Secondly, 0.6, 0.7 and 0.8 mmol indium chloride, and 3 mmol sodium hydroxide were added into 50 mL deionized (DI) water accompanying stirring for 30 min, respectively. Then the above solutions were transferred into 60 ml stainless steel autoclave, respectively, and maintained at 160 °C for 12 h to obtain In_2O_3 suspension. Thirdly, 0.4, 0.3 and 0.2 mmol MoS_2 precusor (obtained in the first step) was mixed with the above In_2O_3 suspension (obtained in the second step) via stirring for 6 h, respectively, and followed by hydrothermally heated in a stainless steel autoclave at 190 °C for 24 h. The obtained precipitate was washed several times with DI water and ethanol to eliminate the impurity ions, and the In_2O_3@MoS_2 precursors were obtained after drying for 12 h at 80 °C. Fourthly, 200 mg In_2O_3@MoS_2 precursor was homogenized in agate mortar before loaded in a alumina crucible, then the reactant preheated at 500 °C for 3 h. Finally, the powder products (obtained in the fourth step) were treated in the crucible at 700 °C for 48 h, followed by an intermediate grinding at room temperature, heated again at 780 °C for 20 h and cooled down in the furnace, and the $In_2(MoO_4)_3$@In_2O_3 samples obtained. All the heating rates were set at 1 °C/min. For convenience, we defined the name of the above three samples as $In_2(MoO_4)_3$@$5In_2O_3$ (Mo:In = 2:8), $In_2(MoO_4)_3$@$2.5In_2O_3$ (Mo:In = 3:7), $In_2(MoO_4)_3$@$1.25In_2O_3$ (Mo:In = 4:6) according to the molar ratio of Mo/In, respectively.

2.3. Characterizations

The surface morphology of the final product was conducted by a field emission scanning electron microscope (FESEM, Zeiss Gemini 500). The lattice fringe images of $In_2(MoO_4)_3$@In_2O_3 were obtained on a high resolution transmission electron microscopy (TEM, JEM-1011) at an acceleration voltage of 100 kV in combination with energy dispersive X-ray (EDX). The microstructure of the sample was further investigated by X-ray diffraction (XRD), performed on a Bruker D8 diffractometer with Cu K radiation ($\lambda = 0.154$ nm), XPS measurements were recorded with an Termo Scientific Escalab 250xi instrument equipped with a monochromatic Al Kα source. Gas sensing properties were measured by WS-30A gas sensing static measurement system (Wei Sheng Electronics Science and Technology Co., Ltd., Henan Province, China). During the gas-sensing tests, a certain volume of the ethanol was injected into the test chamber. When the resistance of the sensor was stable, the chamber was lifted to introduce the ambient air (the relative humidity was measured by a reference commercial humidity sensor). In this article, the response was defined as S_r ($S_r = R_a/R_g$) for tested gas, where R_a and R_g are the sensor resistances measured in air and target gas atmosphere, respectively. In addition, the resistance rate (ρ) was expressed as this: $R_a/100R_g$.

3. Results and discussion

Fig. 1a gives a general synthesis route. Here, we firstly obtained MoS_2@In_2O_3 precursor after three hydrothermal processes, and then we calcined the precursor in the air directly. Finally, the flower-like $In_2(MoO_4)_3$@In_2O_3 nanocomposites could be obtained. From the Fig. 1b, we can obviously see that a large number MoS_2@In_2O_3 nanospheres were successfully fabricated, the average diameter of the nanospheres is about 200–300 nm. Then, the MoS_2@In_2O_3 nanospheres were calcined directly in air at very low

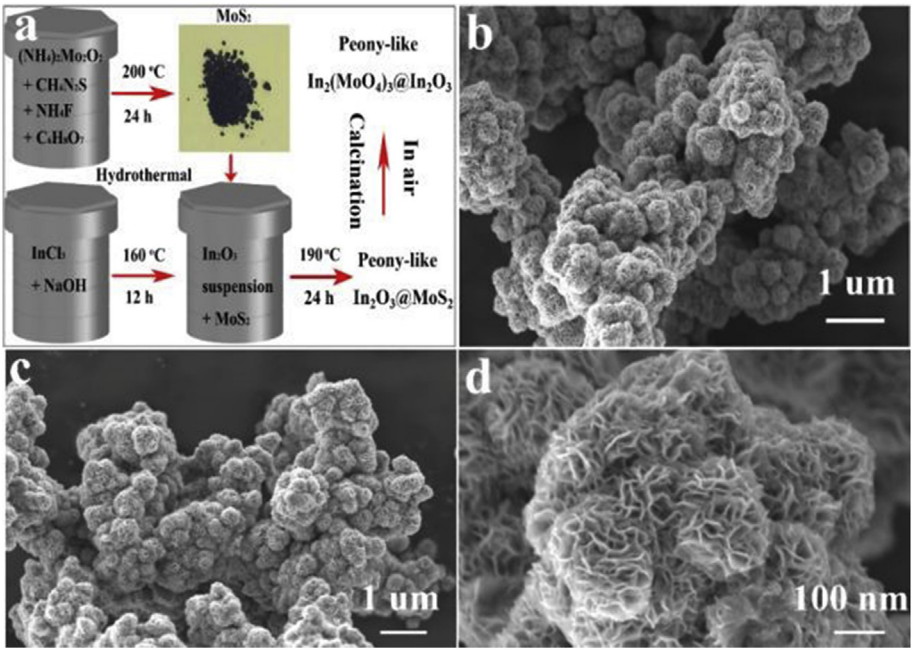

Fig. 1. (a) Sketch of the general synthesis processes. (b) The low magnitude SEM image of $MoS_2@In_2O_3$ precursor. (c) The low magnitude SEM image of calcined $MoS_2@In_2O_3$ precursor that is the SEM image of $In_2(MoO_4)_3@In_2O_3$. (d) The high magnitude SEM image of $In_2(MoO_4)_3@In_2O_3$ nanocomposites.

heating/cooling rates. It can be observed that the calcined products have similar morphology to the $MoS_2@In_2O_3$ precursor, still keeping the beautiful shape of flower, see Fig. 1c. Interestingly, the 3D (three dimensional) $In_2(MoO_4)_3@In_2O_3$ nanosphere is consisted of many tightly aggregated 2D nanoflakes, which are very similar to the petals of a peony flower, as shown in the high magnitude SEM of the Fig. 1d. Form the above results, we can find that the calcination processes have no evident influence on the morphology of the final products.

Fig. 2a shows a TEM image of the $In_2(MoO_4)_3@In_2O_3$ nanocomposites. By this measurement, we obtained detailed information of the structural features of the as-prepared $In_2(MoO_4)_3@In_2O_3$ nanocomposites. It can be clearly observed that In_2O_3 phase is closely attached to the surface of $In_2(MoO_4)_3$ phase. Fringe spacing of 0.292 nm corresponds to the (222) plane of In_2O_3 and the fringe spacing of 0.272 nm matches well with the (422) plane of $In_2(MoO_4)_3$ [25,27]. Thus, the In_2O_3 have been incorporated into $In_2(MoO_4)_3$ well. Fig. 2b shows the XRD pattern of the as-synthesized sample. Strong and sharp diffraction peaks suggest a well crystallized of $In_2(MoO_4)_3@In_2O_3$ nanocomposites. The obvious diffraction peaks locate at $2\theta = 18.8°$, 22.0°, 24.8°, 26.6°, and 32.8° can be ascribed to the (220), (311), (321), (400) and (422) planes, which agree well with the standard patterns of the $In_2(MoO_4)_3$, and consistent with the values in the standard card of PDF#21-0908. Besides, other strong diffraction peaks that is $2\theta = 30.5°$, 35.4°, 41.8°, 45.6°, 51.0° and 60.6° can be easily indexed to the (222), (400), (332), (431), (440) and (622) planes in the hexagonal phase of In_2O_3 (PDF#44-1087) [30]. Suggesting the successful preparation of $In_2(MoO_4)_3@In_2O_3$ nanocomposites. The average crystal sizes of $In_2(MoO_4)_3$ and In_2O_3 nanocomposites have been calculated by Scherrer's formulation ($D = K\lambda/B\cos\theta$) [2,4]. To $In_2(MoO_4)_3$, by applying Scherrer's equation to the (220), (400), and (422) peaks, the average crystallite size was calculated to be 43.9 ± 1.8 nm, and to In_2O_3 ((222), (400), (440), (622)), the average crystallite size is 58.1 ± 22.1 nm. So, the grain size become be smaller when existing $In_2(MoO_4)_3$ phase. No other peaks are found in the patterns, illustrating the purity of $In_2(MoO_4)_3@In_2O_3$. By EDX measurement, we further verify the constituent elements of the $In_2(MoO_4)_3@In_2O_3$ nanocomposites, and the EDX (Fig. 2c) results indicate that the $In_2(MoO_4)_3@2.5In_2O_3$ sample are consisted of O, Mo and In, and the atomic ratio of In and Mo is ~2.59, which is approach to the initial molar ratio, indicating that there is little loss of In and Mo in the growing processes. Again, to investigate the surface elements and chemical states of the $In_2(MoO_4)_3@In_2O_3$ nanocomposites, high resolution XPS spectra were carried out. All the elements such as Mo, In, O, and C can be clearly detected in $In_2(MoO_4)_3@2.5In_2O_3$ nanocomposites (see Fig. S1, Supporting Information). In Fig. 2d, the two peaks at 232.4 eV and 235.7 eV belong to the doublet Mo $3d_{5/2}$ and Mo $3d_{3/2}$, respectively, which is attributed to the Mo^{5+} of $In_2(MoO_4)_3$ phase [21]. Fig. 2e shows the XPS spectrum of In 3d state, which indicates the peaks (444.8 eV and 452.4 eV) corresponding to the In $3d_{5/2}$ and In $3d_{3/2}$, respectively. The peak difference between In $3d_{3/2}$ and In $3d_{5/2}$ is 7.6 eV, which manifests that In element exists mainly in the form of In^{3+} in $In_2(MoO_4)_3@In_2O_3$ [30]. Fig. 2f gives the XPS spectrum of O 1s, two peaks located at 529.2 eV and 531.0 eV can be seen from the sample, similar results has been reported somewhere [31]. In addition, the percentages of the O^- and O^{2-} are 81.49% and 18.51%, respectively. Obviously, the ratio of O^- is higher than O^{2-}, which means that the existence of surface defects makes $In_2(MoO_4)_3@In_2O_3$ adsorbs and ionizes more oxygen, leading to significant enhancement of the sensor response [31]. The peak located at 529.2 eV can be attributed to the lattice oxygen in the as-prepared product structure embraced by In and Mo element, and the peak at 531.0 eV can be assigned to the oxygen defects in the metal oxide regions [32].

Adequate amount of samples such as $In_2(MoO_4)_3@5In_2O_3$, $In_2(MoO_4)_3@2.5In_2O_3$, $In_2(MoO_4)_3@1.25In_2O_3$ and pristine In_2O_3 was mixed with several drops of deionized water to form mash, respectively. Then, the mash was evenly coated on an alumina ceramic tube in turn, and dried at 60 °C for overnight. Fig. 3a illustrates that the ceramic tube (length is 4 mm, diameter is 1 mm) was positioned with one Pt electrode and two Pt wires on each side. A Ni–Cr alloy wire was inserted into the ceramic tube as a heating part to modulate the working temperature of the sensor. In

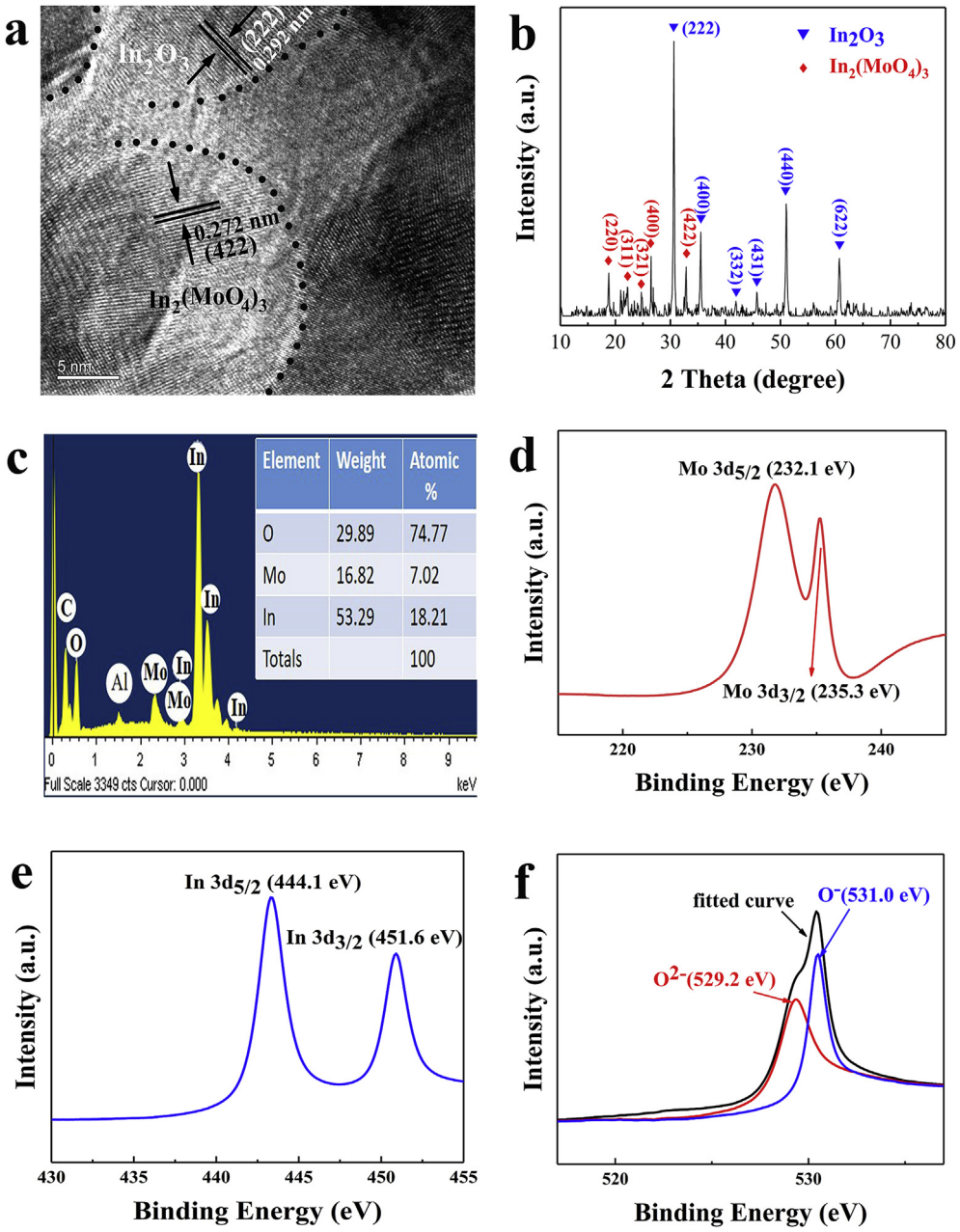

Fig. 2. (a) HRTEM image of $In_2(MoO_4)_3$@2.5In_2O_3 sample. (b) XRD pattern of $In_2(MoO_4)_3$@2.5In_2O_3 sample. (c) The EDX spectrum of $In_2(MoO_4)_3$@2.5In_2O_3. (d), (e) and (f) are XPS spectra Mo 3d, In 3d and O 1s core level XPS spectrum.

addition, Fig. 3a also shows that the testing circuit and a real home-made sensor, which has been attached to the pedestal of a sensor testing unit.

The working temperature is a very crucial parameter for gas sensors based on MOSC according to the literature. To investigate the optimum operating temperature of as-prepared devices, we explore the functional relationship between the sensor response and the operating temperature of the gas sensors based on $In_2(MoO_4)_3$@5In_2O_3, $In_2(MoO_4)_3$@2.5In_2O_3, $In_2(MoO_4)_3$@1.25 In_2O_3 and pristine In_2O_3 from range of 25–350 °C at 50 ppm ethanol, respectively. From the Fig. 3b, we can observe that all the devices show a close temperature-dependent characterization, which might be caused by kinetics and mechanics of gas reaction both chemisorbed oxygen and reducing gas to *n*-type semiconductor of In_2O_3. Evidently, however, the response of the device base on $In_2(MoO_4)_3$@2.5In_2O_3 reaches the maximum values of resistance rate ($\rho = 0.81$) at the 300 °C, and then decrease rapidly with further increase of the temperature, which is due to the competing desorption of the chemisorbed oxygen [31,32]. Again, phase transition is another important reason because it has been reported that the monoclinic to orthorhombic phase transition of $In_2(MoO_4)_3$ is around 340 °C [26]. Therefore, 300 °C is the optimum operating temperature for the $In_2(MoO_4)_3$@In_2O_3 gas sensor. In addition, $In_2(MoO_4)_3$@2.5In_2O_3 exhibits the highest resistance rate among all the samples, which manifest that the ratio of Mo and In have significantly influence on the gas sensing performances. Fig. 3c gives the dynamic response and recovery properties of obtained sensors based on $In_2(MoO_4)_3$@2.5In_2O_3 and pristine In_2O_3

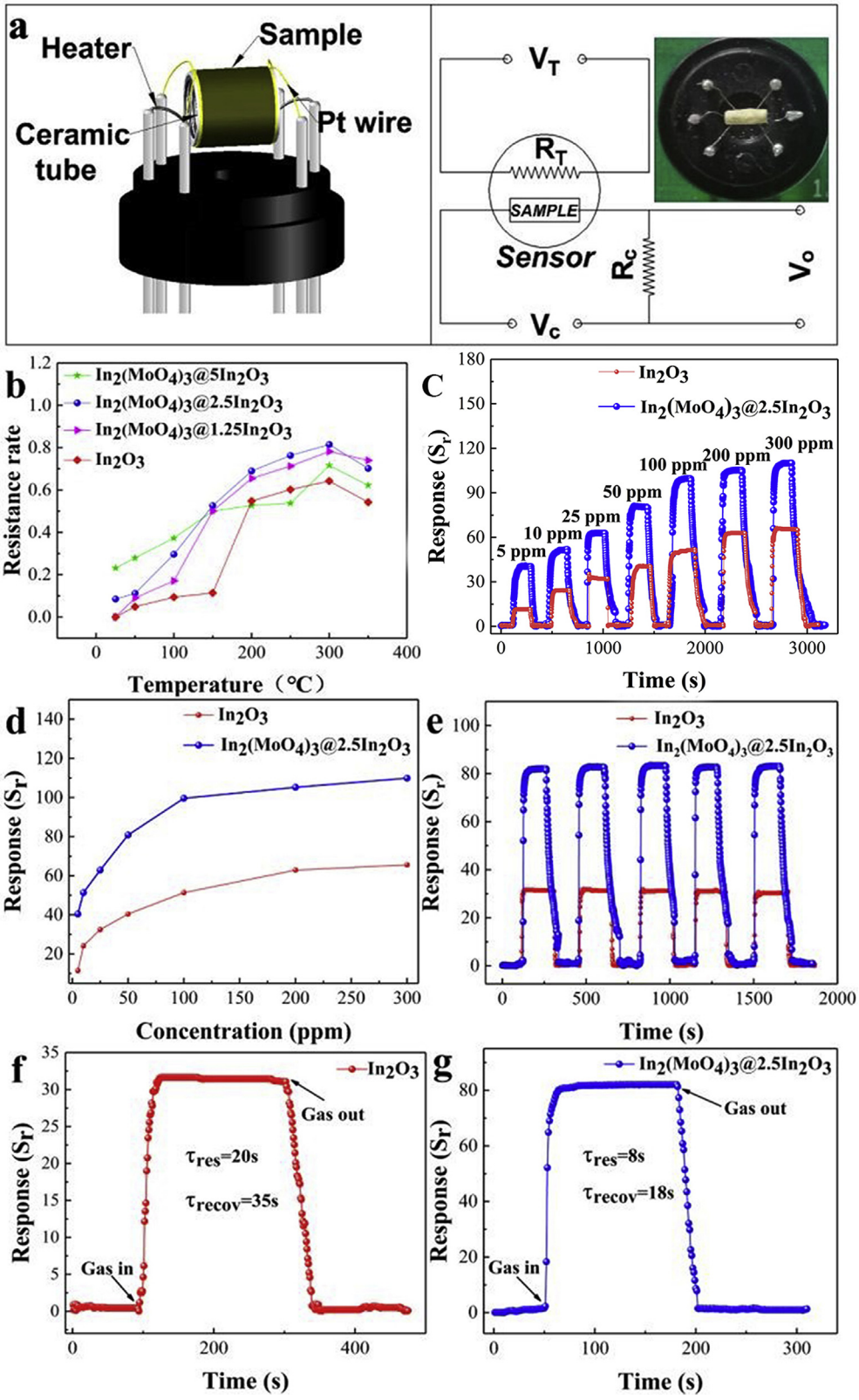

Fig. 3. (a) The gas sensor structure, wire connection, the schematic of the testing circuit, and the inset shows a photo of a home-made sensor. (b) Sensing performances of the gas sensors towards 50 ppm ethanol gas at different operating temperatures. (c) Response of the ethanol gas sensor to different concentrations (from 5 to 300 ppm) at 300 °C. (d) Response *vs* gas concentration for $In_2(MoO_4)_3@2.5In_2O_3$ and In_2O_3 sensors. (e) Repeatability test of the $In_2(MoO_4)_3@2.5In_2O_3$ and pure In_2O_3 sensors to 50 ppm of ethanol at 300 °C. (f) and (g) response and recovery characteristics of the pure In_2O_3 and $In_2(MoO_4)_3@2.5In_2O_3$ sensors toward 50 ppm at 300 °C, respectively.

nanoparticles to different ethanol vapor concentrations (from 5 to 300 ppm) at 300 °C. With the increase of the ethanol concentration, the responses of the two sensors increase sharply. Obviously, however, the sensor based on $In_2(MoO_4)_3$@2.5In_2O_3 shows the best response and recovery characterization to ethanol gas, especially the response value has a sharp promotion after 50 ppm, see Fig. 3d. We suggest that with the increasing concentration of ethanol, the response of gas sensor was determined by the surface reaction rate. It can be also demonstrated that the hierarchical nanostructure of the increases more cusps, which can act as active sites, on the surface of the $In_2(MoO_4)_3$@In_2O_3 nanocomposites. With the gradual increase of concentration of ethanol, the response of gas sensors shows the tendency of smoothness due to the insufficient active sites. When the ethanol concentration reach to 300 ppm, the response gradually approaches the status of saturation, see Fig. 3d. The detailed responses of $In_2(MoO_4)_3$@2.5In_2O_3 and In_2O_3 based sensors are listed in Table 1. From the table, we can conclude that the sensor based on $In_2(MoO_4)_3$@2.5In_2O_3 shows approximately 2 times higher response than pure In_2O_3 based sensor, therefore, the $In_2(MoO_4)_3$@In_2O_3 sensor has great application prospect. Fig. 3e shows a typical repeatability test of the $In_2(MoO_4)_3$@2.5In_2O_3 and pure In_2O_3 sensors to 50 ppm of ethanol at 300 °C, respectively. It can be found that the response ($S_r = 81$) of $In_2(MoO_4)_3$@2.5In_2O_3 sensor is much higher than that ($S_r = 30$) of In_2O_3 sensors, because the hierarchical flower shaped nanostructures lead to the increase of specific surface area ratio and more cusps on the surface of the $In_2(MoO_4)_3$@In_2O_3 nanocomposites.

In addition, the optimum the molar ratio of Mo/In plays the best synergy effect [26]. Fig. 3f and g compares the response time (τ_{res}) and recovery time (τ_{recov}) of the pristine In_2O_3 sensor and $In_2(MoO_4)_3$@2.5In_2O_3 sensor to 50 ppm ethanol at 300 °C, which are the vital performance parameters for gas sensors. The τ_{res} of pristine In_2O_3 sensor is 20 s, which is slower than that (8 s) of $In_2(MoO_4)_3$@2.5In_2O_3 sensor. But the $In_2(MoO_4)_3$@2.5In_2O_3 sensor take a very short time ($\tau_{recov} = 18$ s) to recover its initial resistance state. On the contrary, the In_2O_3 sensor needs $\tau_{recov} = 35$ s. According to the recent published papers, the responses (τ_{res} and τ_{recov}) of $In_2(MoO_4)_3$@2.5In_2O_3 sensor is smaller than that of pure In_2O_3, MoO_3 and their hybrids gas sensor, the details were listed in the Table S1, see Supporting Information. The above results suffice to prove that the response and recovery time towards alcohol gas can be significantly improved by fabricating $In_2(MoO_4)_3$@In_2O_3 nanocomposites, because the interface of heterostructures between $In_2(MoO_4)_3$ phase and In_2O_3 phase can activate the conductive electrons.

As an outstanding electronic device, stability, especially working in harsh conditions, is one of the most important evaluation criteria. To estimate the long-term cycling stability of our home-made sensor, the transient sensing responses of the sensor based on $In_2(MoO_4)_3$@2.5In_2O_3 was measured to 50 ppm ethanol at 300 °C. Here, we keep the fabricated device in ambient for 1 day, 30 days, 60 days and 90 days, respectively. Fig. 4a–c give the long-term reliable performance of the $In_2(MoO_4)_3$@In_2O_3 sensor at 30, 60, 90 days in 80% relative humidity (RH), and the device performance on first day was given in Fig. S2, Supporting Information. It can be observed that the $In_2(MoO_4)_3$@In_2O_3 sensor maintain its original response amplitude without significant attenuation upon five successive cycles, which suggested that the $In_2(MoO_4)_3$@In_2O_3 nanocomposites possesses a strong robustness. To deeply analysis the alteration amplitude of the responses for the sensor based on $In_2(MoO_4)_3$@2.5In_2O_3. As shown in Fig. 4d, we draw the S_r-Time bar chart, it can be noted that the alteration amplitude of the response controlled within 6.2%. For comparison, the long-term reliability of In_2O_3 sensor for 5 days, 15 days and 30 days are investigated as depicted in 80% relative humidity (RH), see Fig. S3 to S5 (Supporting Information). However, it can be found that the reliability of In_2O_3 sensor begin to deteriorate after 15 days, see Fig. S6 in Supporting Information. We attributed the long term stability of the $In_2(MoO_4)_3$@In_2O_3 sensor to the existing of $In_2(MoO_4)_3$ phase, because $In_2(MoO_4)_3$ is an important thermal stability compound with negative thermal expansion and high electric conductivity characteristics [27]. In addition, the responses of $In_2(MoO_4)_3$@In_2O_3 sensor was measured at different RH such as 40%, 60%, 80% and 95% for 50 ppm, as shown in Fig. 4e. Evidently, there is no significant alteration of the responses (80.7) from 40% to 80% RH, the gas response of $In_2(MoO_4)_3$@In_2O_3 sensor maintain the pristine value as the humidity increases from 40% to 80% RH due to the enhanced surface reaction sites, but an obvious decrease of response of 65.9 can be observed till to 95% RH. We suggest that the decrease of the resistance can be ascribed to the water molecules dissociate at room temperature through a chemisorption process and donate electrons to In_2O_3 [33,34]. In addition, water molecules compete with the chemisorption ethanol molecules, which reduces superficial concentrations hence hamper the catalytic oxidation of ethanol [35,36].

Again, the gas sensing selectivity of the $In_2(MoO_4)_3$@2.5In_2O_3 and pristine In_2O_3 sensor was probed by exposing other VOCs vapors with the same concentration of 50 ppm at optimum operating temperature of 300 °C, respectively (Fig. 4f). The responses of ethylene glycol, acetone, benzene, NH_3 and methanol were 2.2, 2.7, 1.5, 1.1, 2.7 and 80.5, whereas 1.7, 1.9, 1.2, 1.0, 2.2, and 30.7 for In_2O_3, respectively. On comparison, it can be seen that $In_2(MoO_4)_3$@2.5In_2O_3 sensor has a much higher response to all the test gases than pure In_2O_3. This clearly indicates that the $In_2(MoO_4)_3$@2.5In_2O sensor exhibits excellent selectivity toward ethanol than that of pure In_2O_3 based.

On the basis of the above results and further XPS analysis as presented in Fig. 5, we give a possible response mechanism. It is well known that In_2O_3 is an *n*-type semiconductor material, when it is exposed to fresh air, the chemisorbed oxygen molecules on the surface will become O^{2-}, O_2^- and O^- through capturing electrons from the conduction band (E_c) of In_2O_3, giving rise to decrease of carriers and increase the depletion layer [37,38], and the gas sensing mechanism of $In_2(MoO_4)_3$@In_2O_3 nanocomposites is schematic illustrated in Fig. 5a. So, the resistance of In_2O_3 would be in high level, the reaction process can be described as the following,

$$O_{2\ (g)} + 2e^- = 2O^-,\ O_2^- + e^- = 2O^-,\ O^- + e^- = O^{2-} \quad (1)$$

When the $In_2(MoO_4)_3$@In_2O_3 sensor is exposed in ethanol gas, the reactive oxygen O^- will react with C_2H_6O molecules. The process could be expressed in the reaction as follows:

$$C_2H_5OH + O^{2-} \rightarrow CH_3CHO + H_2O_{(gas)} + 2e^- \quad (2)$$

$$CH_3CHO + 5O^{2-} \rightarrow 2CO_2 + 2H_2O_{(gas)} + 10e^- \quad (3)$$

Reactions 2 and 3 release electrons back to the E_c of In_2O_3, resulting in an increase in electron concentration and a decrease in resistance of device. Therefore, abundant active reaction sites and

Table 1
The responses of $In_2(MoO_4)_3$@2.5In_2O_3 and In_2O_3 sensors at 300 °C.

Materials	Concentration (ppm)						
	5	10	25	50	100	200	300
$In_2(MoO_4)_3$@In_2O_3	40.4	51.3	62.8	80.7	99.4	105.1	110.0
In_2O_3	11.5	24.2	32.1	40.4	50.7	62.9	65.6

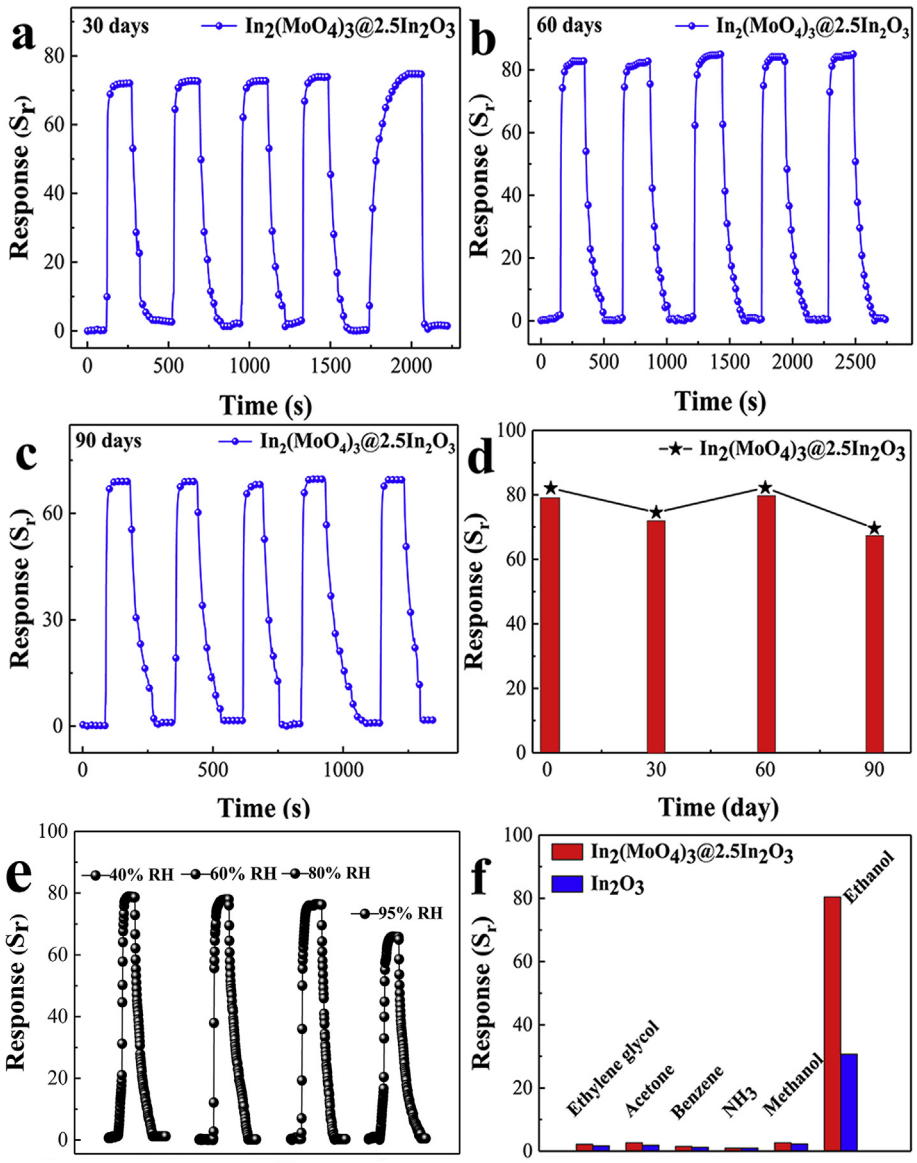

Fig. 4. (a), (b) and (c) response stability of $In_2(MoO_4)_3$@In_2O_3 sensor towards ethanol at 300 °C lasting for 30 days, 60 days and 90 days, respectively. (d) the bar chart of the long term stability of $In_2(MoO_4)_3$@In_2O_3 sensor. (e) Typical response curves of the $In_2(MoO_4)_3$@In_2O_3 sensor to various RH values. (f) The selectivity comparison of $In_2(MoO_4)_3$@2.5In_2O_3 and pure In_2O_3 sensors for different target gases at 300 °C.

small grain size are preferred to promote a dramatic resistance change when target gases are injected. Here, the enhancement of the gas response and durability of the sensor based on $In_2(MoO_4)_3$@In_2O_3 hierarchical flower-like nanocomposites are likely to ascribe the changes in crystallite size as mentioned above, and existing the $In_2(MoO_4)_3$ phase, because the sensitivity could be greatly enhanced when the grain size reduced to a scale [39,40].

To deeply investigate the change of O^- on the surface of $In_2(MoO_4)_3$@In_2O_3, XPS analysis after measurement was considered also. From the Fig. 5b, it can be evidently seen that the O^- content (55.34%) of after measurement $In_2(MoO_4)_3$@In_2O_3 is much lower than that of as-prepared (81.49%). According to the sensing mechanism of MOC_S sensor, we suggest that the sharp declination of O^- is partially ascribed to the slight deterioration of the $In_2(MoO_4)_3$@In_2O_3 and the decreased defects amount [41].

4. Conclusions

In summary, we successfully synthesized the peony shaped $In_2(MoO_4)_3$@In_2O_3 nanocomposites via facile hydrothermal and calcination methods. And the composites were utilized as a highly sensitive material for ethanol gas sensor applications. The $In_2(MoO_4)_3$@In_2O_3 sensor exhibits excellent ethanol sensing performances, including enhanced gas response, selectivity, and long-term stability in harsh conditions towards ethanol with rapid response and recovery at optimum working temperature of 300 °C, which is better than that of pristine In_2O_3 gas sensor. We suggest that the superior sensing properties can be attributed to the first introduction of $In_2(MoO_4)_3$ phase into $In_2(MoO_4)_3$@In_2O_3 sensor. Therefore, our results would make a meaningful contribution towards the fabrication of $In_2(MoO_4)_3$@In_2O_3 gas, showing its great promising prospect for commercial applications in ethanol detection.

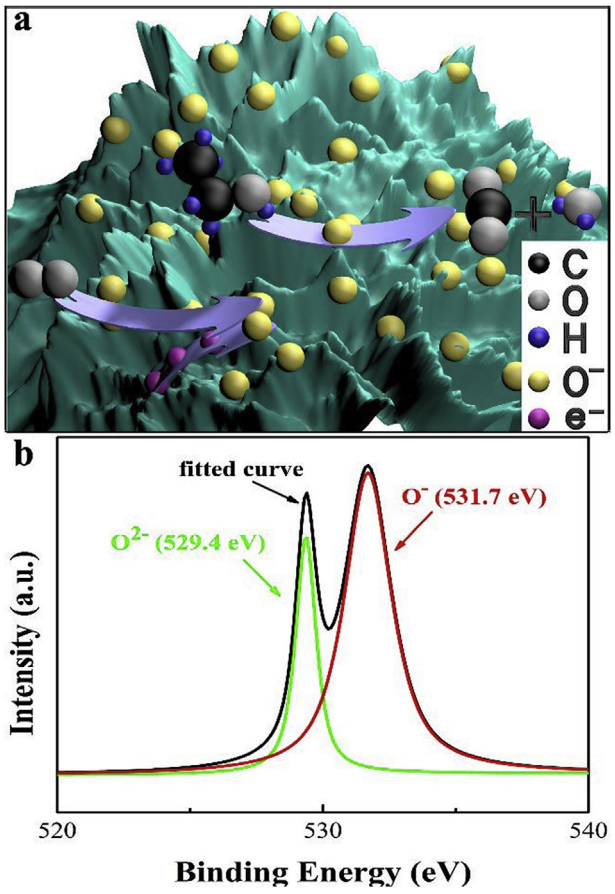

Fig. 5. Schematic diagram of the sensing reaction mechanism of (a) gas sensing mechanism of $In_2(MoO_4)_3$@In_2O_3 nanocomposites. (b) XPS spectrum of O 1s of $In_2(MoO_4)_3$@In_2O_3 surface after measurement.

Conflicts of interest

There are no conflicts to declare.

Acknowledgements

The authors acknowledge financial supports from the National Natural Science Foundation of China (Grant No. 51227804), the Natural Science Foundation of Jiangsu Province (BK20170330) and the Postdoctoral Scientific Research Foundation of Qingdao. This project was also funded by the Collaborative Innovation Center of Suzhou Nano Science and Technology.

Appendix A. Supplementary data

Supplementary data to this article can be found online at https://doi.org/10.1016/j.jallcom.2019.06.369.

References

[1] O. Chmela, J. Sadilek, G. Domenech-Gil, J. Sama, J. Somer, R. Mohan, A. Romano-Rodriguez, J. Hubalek, S. Vallejos, Selectively arranged single-wire based nanosensor array systems for gas monitoring, Nanoscale 10 (2018) 9087–9096.
[2] C.J. Chang, C.Y. Lin, J.K. Chen, Ce-doped ZnO nanorods based low operation temperature NO_2 gas sensors, Ceram. Int. 40 (2014) 10867–10875.
[3] C.K. Lin, C.Y. Chen, C.J. Chang, et al., Gas sensors with porous three-dimensional framework using TiO_2/polymer double-shell hollow microsphere, Thin Solid Films (520) (2011) 1546–1553.
[4] C.J. Chang, S.T. Hung, C.K. Lin, C.Y. Chen, E.H. Kuo, Selective growth of ZnO nanorods for gas sensors using ink-jet printing and hydrothermal processes, Thin Solid Films (519) (2010) 1693–1698.
[5] Q. Xu, X. Liu, B. Wan, Z. Yang, F. Li, J. Lu, G. Hu, C. Pan, Z.L. Wang, In_2O_3 nanowire field-effect transistors with sub-60 mV/dec subthreshold swing stemming from negative capacitance and their logic applications, ACS Nano 12 (2018) 9608–9616.
[6] W. Huang, B. Zhu, S.Y. Chang, S. Zhu, P. Cheng, Y.T. Hsieh, L. Meng, R. Wang, C. Wang, C. Zhu, C. McNeill, M. Wang, Y. Yang, High mobility indium oxide electron transport layer for an efficient charge extraction and optimized nanomorphology in organic photovoltaics, Nano Lett. 18 (2018) 5805–5811.
[7] B.S. Li, B.J. Xi, Z.Y. Feng, Y. Lin, J.C. Liu, J.K. Feng, Y.T. Qian, S.L. Xiong, Hierarchical porous nanosheets constructed by graphene-coated, interconnected TiO_2 nanoparticles for ultrafast sodium storage, Adv. Mater. 30 (2018) 1705788.
[8] R. Paniagua-Dominguez, Y.F. Yu, E. Khaidarov, S. Choi, V. Leong, R.M. Bakker, X. Liang, Y.H. Fu, V. Valuckas, L.A. Krivitsky, A.I. Kuznetsov, A metalens with a near-unity numerical aperture, Nano Lett. 18 (2018) 2124–2132.
[9] R. Haldavnekar, K. Venkatakrishnan, B. Tan, Non plasmonic semiconductor quantum SERS probe as a pathway for in vitro cancer detection, Nat. Commun. 9 (2018) 3065.
[10] B. Sacépé, J. Seidemann, F. Gay, K. Davenport, A. Rogachev, M. Ovadia, K. Michaeli, M.V. Feigel'man, Low-temperature anomaly in disordered superconductors near B_{c2} as a vortex-glass property, Nat. Phys. 15 (2018) 48–53.
[11] H. Yang, X. Bai, P. Hao, J. Tian, Y. Bo, X. Wang, H. Liu, A simple gas sensor based on zinc ferrite hollow spheres: highly sensitivity, excellent selectivity and long-term stability, Sens. Actuators, B 280 (2019) 34–40.
[12] Z. Zhang, M. Xu, L. Liu, X. Ruan, J. Yan, W. Zhao, J. Yun, Y. Wang, S. Qin, T. Zhang, Novel SnO_2@ZnO hierarchical nanostructures for highly sensitive and selective NO_2 gas sensing, Sens. Actuators, B 257 (2018) 714–727.
[13] B. Zhang, W. Fu, X. Meng, A. Ruan, P. Su, H. Yang, Enhanced ethanol sensing properties based on spherical-coral-like SnO_2 nanorods decorated with α-Fe_2O_3 nanocrystallites, Sens. Actuators, B 261 (2018) 505–514.
[14] K. Xu, S. Tian, J. Zhu, Y. Yang, J. Shi, T. Yu, C. Yuan, Enhanced ethanol sensing properties based on spherical-coral-like SnO_2 nanorods decorated with α-Fe_2O_3 nanocrystallites, Nanoscale 10 (2018) 20761–20771.
[15] R. Malik, V.K. Tomer, T. Dankwort, Y.K. Mishra, L. Kienle, Cubic mesoporous Pd–WO_3 loaded graphitic carbon nitride (g-CN) nanohybrids: highly sensitive and temperature dependent VOC sensors, J. Math. Chem. 6 (2018) 10718–10730.
[16] E. Çiftyürek, K. Sabolsky, E.M. Sabolsky, High temperature selective sensing of hydrogen with MgO-modified $SrMoO_4$ micro-fibers, Sens. Actuators, B 249 (2017) 296–310.
[17] D.G. Jiang, W.H. Song, J.W. Lu, et al., Highly selective ethanol In_2O_3-based gas sensor, Mater. Res. Bull. 42 (2007) 228–235.
[18] M.M.Y.A. Alsaif, M.R. Field, B.J. Murdoch, T. Daeneke, K. Latham, A.F. Chrimes, A.S. Zoolfakar, S.P. Russo, J.Z. Ou, K. Kalantar-zadeh, Substoichiometric two-dimensional molybdenum oxide flakes: a plasmonic gas sensing platform, Nanoscale 6 (2014) 12780–12791.
[19] C.H. Feng, X. Li, J. Ma, Y.F. Sun, C. Wang, P. Sun, J. Zheng, G.Y. Lu, Facile synthesis and gas sensing properties of In_2O_3-WO_3 heterojunction nanofibers, Sensor. Actuator. B Chem. 2015 (209) 622–629.
[20] F.X. Ji, X.P. Ren, X.Y. Zheng, Y.C. Liu, L.Q. Pang, J.X. Jiang, S.Z. Liu, 2D-MoO_3 nanosheets for superior gas sensors, Nanoscale 8 (2016) 8696–8703.
[21] E. Ciftyürek, K. Sabolsky, E.M. Sabolsky, Molybdenum and tungsten oxide based gas sensors for high temperature detection of environmentally hazardous sulfur species, Sens. Actuators, B 237 (2016) 262–274.
[22] E. Çiftyürek, K. Sabolsky, E.M. Sabolsky, High temperature selective sensing of hydrogen with MgO-modified $SrMoO_4$ micro-fibers, Sens. Actuators, B 249 (2017) 296–310.
[23] J.T. Li, L.W. Wang, H.J. Liu, J. Zhao, X. Li, H. Wei, Y.F. Han, Synthesis and enhanced toluene gas sensing properties of 1-D α-MoO_3/$Fe_2(MoO_4)_3$ heterostructure, J. Alloy. Comp. 694 (2017) 939–945.
[24] J.W. Ma, H.Q. Fan, H.L. Tian, X.H. Ren, C. Wang, S. Gao, W.J. Wang, Ultrahigh sensitivity and selectivity chlorine gas sensing of In_2O_3 hollow microtubules by bio-template method with degreasing cotton, Sens. Actuators, B 262 (2018) 17–25.
[25] B.A. Marinkovic, M. Ari, P.M. Jardim, R.R. de Avillez, F. Rizzo, F.F. Ferreira, $In_2Mo_3O_{12}$: a low negative thermal expansion compound, Thermochim. Acta 499 (2010) 48–53.
[26] E. Filipek, I. Rychlowska-Himmel, A. Paczesna, Thermal stability of $In_2(MoO_4)_3$ and phase equilibria in the MoO_3–In_2O_3 system, J. Therm. Anal. Calorim. 109 (2012) 711–716.
[27] L. Young, P.T. Alvarez, H.F. Liu, C. Lind, E.J. Inorg, Extremely low temperature crystallization in the $A_2M_3O_{12}$ family of negative thermal expansion,Mater, Chem. 8 (2016) 1251–1256.
[28] A. Arfaoui, A. Mhamdi, D. Jlidi, S. Belgacem, Physical and ethanol sensing properties of sprayed $Fe_2(MoO_4)_3$ thin films, J. Alloy. Comp. 719 (2017) 392–400.
[29] Z. Lin, M. Xu, P. Fu, Q. Deng, Crystal plane control of 3D iron molybdate and the facet effect on gas sensing performances, Sens. Actuators, B 254 (2018) 755–762.
[30] D. Khim, Y.H. Lin, S. Nam, H. Faber, K. Tetzner, R. Li, Q. Zhang, J. Li, X. Zhang, T.D. Anthopoulos, Modulation-doped In_2O_3/ZnO heterojunction transistors processed from solution, Adv. Mater. 29 (2017) 1605837.

[31] S. Yan, J.Z. Xue, Q.S. Wu, Synchronous synthesis and sensing performance of α-Fe_2O_3/SnO_2 nanofiber heterostructures for conductometric C_2H_5OH detection, Sens. Actuators, B 275 (2018) 322–331.
[32] M. Ikrama, Y. Liu, H. Lv, L. J Liu, A.U. Rehman, K. Kan, W. J Zhang, L. He, Y. Wang, R. H Wang, K.Y. Shi, 3D-multilayer MoS_2 nanosheets vertically grown on highly mesoporous cubic In_2O_3 for high-performance gas sensing at room temperature, Appl. Surf. Sci. 466 (2019) 1–11.
[33] S.H. He, W.D. Li, L. Feng, W. Yang, Rational interaction between the aimed gas and oxide surfaces enabling high-performance sensor: the case of acidic α-MoO_3 nanorods for selective detection of trimethylamine, J. Alloy. Comp. 783 (2019) 574–582.
[34] J. Ma, H. Fan, H. Tian, X. Ren, C. Wang, S. Gao, W. Wang, Ultrahigh sensitivity and selectivity chlorine gas sensing of In_2O_3 hollow microtubules by bio-template method with degreasing cotton, Sens. Actuators, B 262 (2018) 17–25.
[35] Y.J. Jeong, W.T. Koo, J.S. Jang, D.H. Kim, H.J. Cho, I.D. Kim, Chitosan-templated Pt nanocatalyst loaded mesoporous SnO_2 nanofibers: a superior chemiresistor toward acetone molecules, Nanoscale 10 (2018) 13713–13721.
[36] Z. Li, A.A. Haidry, B. Gao, T. Wang, Z.J. Yao, The effect of Co-doping on the humidity sensing properties of ordered mesoporous TiO_2, Appl. Surf. Sci. 412 (2017) 638–647.
[37] N. Illyaskutty, H. Kohler, T. Trautmann, M. Schwotzer, V.P.M. Pillai, Hydrogen and ethanol sensing properties of molybdenum oxide nanorods based thin films: effect of electrode metallization and humid ambience, Sens. Actuators, B 187 (2013) 611–621.
[38] X. Wang, M. Gao, Porous Co_3O_4/SnO_2 quantum dot (QD) heterostructures with abundant oxygen vacancies and Co^{2+} ions for highly efficient gas sensing and oxygen evolution reaction, Nanoscale 10 (2018) 12045–12053.
[39] N. Xie, L. Guo, F. Chen, X. Kou, C. Wang, J. Ma, Y. Sun, F. Liu, X. Liang, Y. Gao, X. Yan, G. Lu, Enhanced sensing properties of SnO_2 nanofibers with a novel structure by carbonization, Sens. Actuators, B 271 (2018) 44–53.
[40] A. Dabiran, P. Chow, C.J. Chang, et al., SnO_2 functionalized AlGaN/GaN high electron mobility transistor for hydrogen sensing applications, Int. J. Hydrogen Energy 37 (2012) 13783–13788.
[41] Y.L. Wang, X.C. Jiang, Y.N. Xia, A solution-phase, precursor route to poly-crystalline SnO_2 nanowires that can Be used for gas sensing under ambient conditions, J. Am. Chem. Soc. 125 (2003) 16176–16177.